A novel imaging algorithm for broadband aperture synthesis data

Christian A. Hummel

ESO, Karl-Schwarzschild-Str. 2, 85748 Garching, Germany

ABSTRACT

I developed a new imaging algorithm allowing the combination of multi-channel interferometric data in a single image. The method is applicable to sources emitting optically thick radiation where the dependence of the source structure on wavelength can therefore be described by a single parameter, i.e. the (local) effective temperature. The result of the imaging process is an intensity map as well as a map of the effective temperature across the source. The advantage of this method over the independent imaging of data in each channel is the benefit of a much better DB ("dirty beam", also PSF) when combining the aperture coverage of each channel over a wide range of wavelengths. I present results from applications to composite spectrum binaries and stellar surfaces of rotating stars based on simulated data.

My imaging algorithm is based on the well known CLEAN method, adding the effective temperature as an additional parameter for each image pixel. This information can be used to scale the PSF in each channel with the blackbody law and subtract it from the combined residual map. Once a cleaned map has been obtained (using regular phase self-calibration techniques) and thus a set of phase-corrected visibilities, individual channel maps are obtained by running the CLEAN restricted to non-zero pixels. The cleaned channel maps together with the total flux spectrum can then be used to estimate the blackbody temperature for each non-zero image pixel, and used for the next iteration of the modified CLEAN algorithm.

Keywords: interferometric imaging, broadband aperture synthesis

1. INTRODUCTION

Interferometric imaging in the optical has come to a crossroads. While efforts to combine a larger number of telescopes have been intense, no routine observations are carried out with more than four. A high point in the quest to improve the aperture coverage came with the first simultaneous combination[1] of six siderostats of the NPOI[2] array, providing 12 of the 15 possible baselines thanks to a hybrid beam combiner design. Subsequently, however, NPOI has reduced the number of simultaneous siderostats due to problems with cross talk.[3]

In marked contrast to radio interferometers, optical interferometers have now often developed a spectroscopic capability covering fractional bandwidths between 20% and 40% in the lowest spectral resolution setting. This leads to significant improvements in the aperture coverage (see Fig. 1) at the expense of having to account for possible changes of the source structure as a function of wavelength if all the channels are to be combined in a single image. This article shows one way to solve this problem.

2. THE THIRD DIMENSION IN IMAGING

Image cubes, with the third axis representing wavelength (or frequency) are of course a well known result of, e.g., integral field unit observations, but not so for spectrally resolved interferometry. Only recently a large effort has resulted in the first impressive image cube of T Leporis[4] derived from AMBER[5]/VLTI[6] H and K-band spectrally-resolved visibilities. Therefore, truly model independent imaging in many separate channels will be more of an exception than the rule in the near future.

However, already a few years ago, this author[1] suggested to combine the data of several spectral channels by describing the wavelength dependence of the source structure in terms of blackbody spectra. This is equivalent

Further author information: (Send correspondence to C.A.H.)
C.A.H.: E-mail: chummel@eso.org, Telephone: +49 (0)89 3200 6151

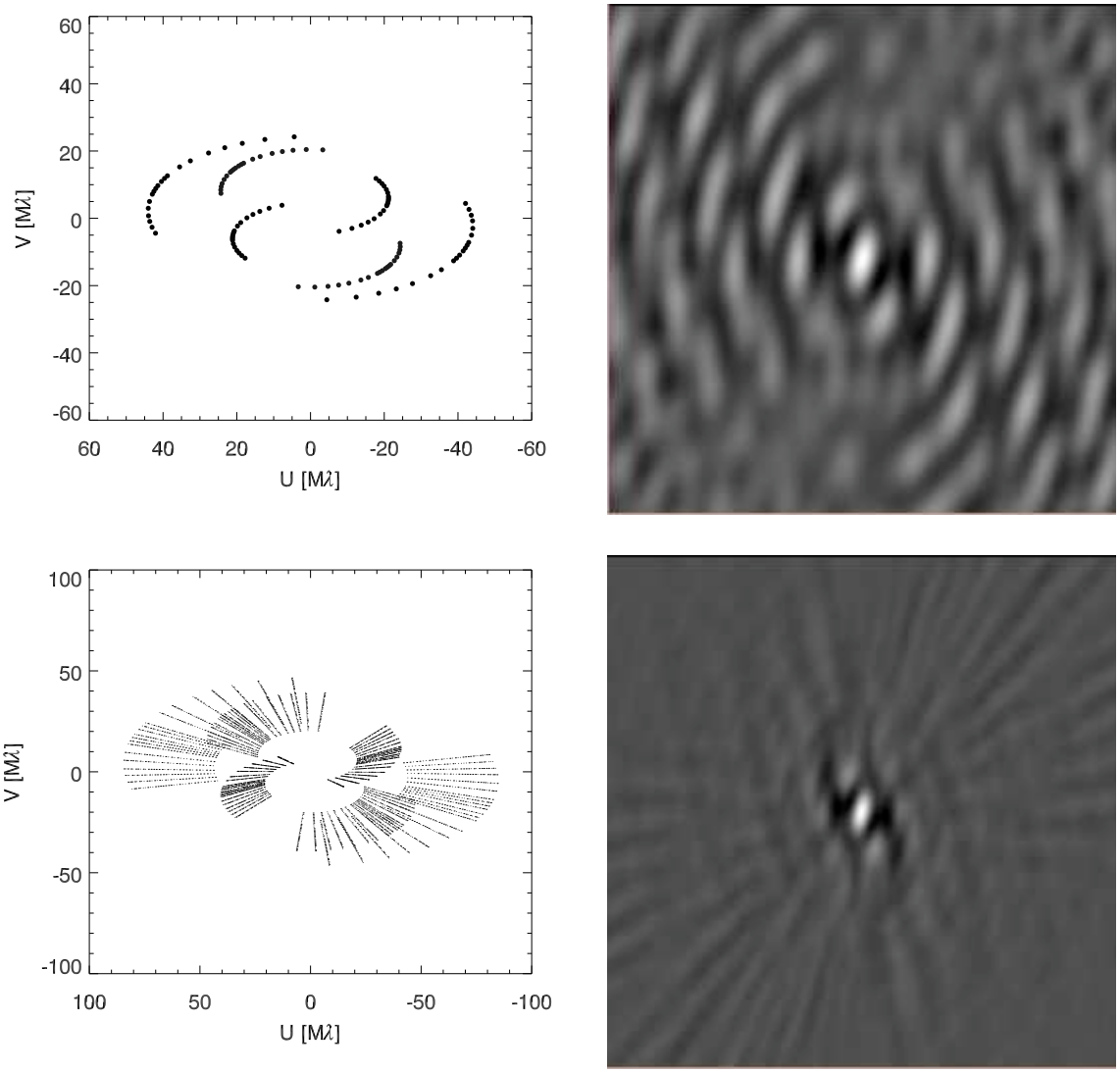

Figure 1. The advantage of multi-channel aperture synthesis. The top panel shows the aperture coverage and resulting "dirty beam" (DB, or PSF) of a 3-station observation in a single spectral channel, while the bottom panel shows a multi-channel (60% fractional bandwidth) observation with the same array.

to constraining, in addition to just one single image, a map of effective temperatures for each source pixel. I implemented this idea by modifying the well known CLEAN deconvolution algorithm as described in the following. The terminology used is adopted from radio interferometry, where a similar technique is used to compensate for the spectral index of optically thin synchrotron radiation in wide band observations (see the documentation for the MIRIAD software at *http://www.atnf.csiro.au/computing/software/miriad/*).

3. MULTI-WAVELENGTH CLEAN

CLEAN iteratively deconvolves a "dirty" map (DM), i.e. the direct Fourier transform of the complex visibility data, from the synthesized beam (DB) by subtracting (a fraction of) the latter centered on the location of the brightest pixel. The subtracted flux is entered as a Dirac function in the clean map (CM). I now assign each CLEAN component an effective (blackbody) temperature based on the location in the map, allowing us to combine all data by being able to compute the entire image cube. Thus I write DM as a sum over all spectral channels j,

$$DM = \sum_j DM_j.$$

Given a (white light) flux f^i of a CLEAN component at iteration i, and its effective temperature T^i, the flux for channel j, f^i_j, is computed using the blackbody radiation law and normalized by the total observed flux in that channel, F_j. The reason for the normalization is the fact that maps are computed from normalized visibilities, not correlated fluxes. The dirty beam of channel j, DB_j, is then multiplied by f^i_j/F_j and subtracted from RM_j. RM is the residual map, which is initially identical to DM. This procedure ensures that the correct fraction of flux is subtracted as a function of wavelength. Thus I compute the residual map at iteration $i+1$ as follows:

$$RM^{i+1} = RM^i - \sum_j \frac{f^i_j}{F_j} DB_j.$$

The algorithm was tested with data from a simulation based on the observation shown in Fig. 1. In Fig. 2 I show the results for a binary with a hot and a cool component which demonstrate the capability of multi-wavelength CLEAN to remove artefacts from the combined image.

Figure 2. Application of multi-wavelength CLEAN based on blackbody radiation to a simulated composite spectrum binary based on the observation shown in Fig. 1. For the map on the left no temperature difference between the components was assumed, while the effective temperature image (middle) shows that the left component has an effective temperature of 10000 K, the right one of 5000 K. Taking these into account, the map on the right shows a much improved dynamic range.

4. DIFFERENCE MAPPING AND PHASE SELF CALIBRATION

Just as in conventional imaging of radio interferometric data, an image deconvolution step is followed by the computation of an improved solution of the visibility phase corrections based on the new model. Here, I implemented a "difference" mapping scheme[7] in which CLEAN components are only extracted from residual maps representing the Fourier transform of the accumulated CLEAN map subtracted from the phase calibrated visibility data. Such a scheme is better suited to the data from optical interferometry due to their sparsity and use of closure phases, by allowing better control over non-linear processes such as CLEAN. Phase self-calibration is performed by solving for station phase corrections which minimize the difference between the observed (random) visibility phase and the model phase. I remove phase wraps by applying a dynamic weight mask to the design matrix of the linear least squares fit which suppresses all baselines except those involving a selection of stations, starting with just one, and increasing to all stations iteratively between new phase solutions.

5. EFFECTIVE TEMPERATURE CALIBRATION

An initial estimate of the effective temperature map can be obtained from the spectral types of the stars and their approximate location in the image, or from partially resolved photometry of the field. Even if only a single value has been adopted for the entire image from fitting a blackbody spectrum to the total flux F, differences in T will have been transformed into differences in f after the first iteration. Obviously, this estimate has to be refined subsequently. The most straightforward way would be to image each channel separately, scale these images with the total flux $F(\lambda)$ and then fit blackbody spectra to the flux of each pixel as a function of wavelength. In order to provide powerful constraints on this procedure (lest I loose the advantage of having combined the data), I adopt the visibility phase calibration from the previous step, and restrict the search of CLEAN for the brightest pixel to those which had flux in the previous step.

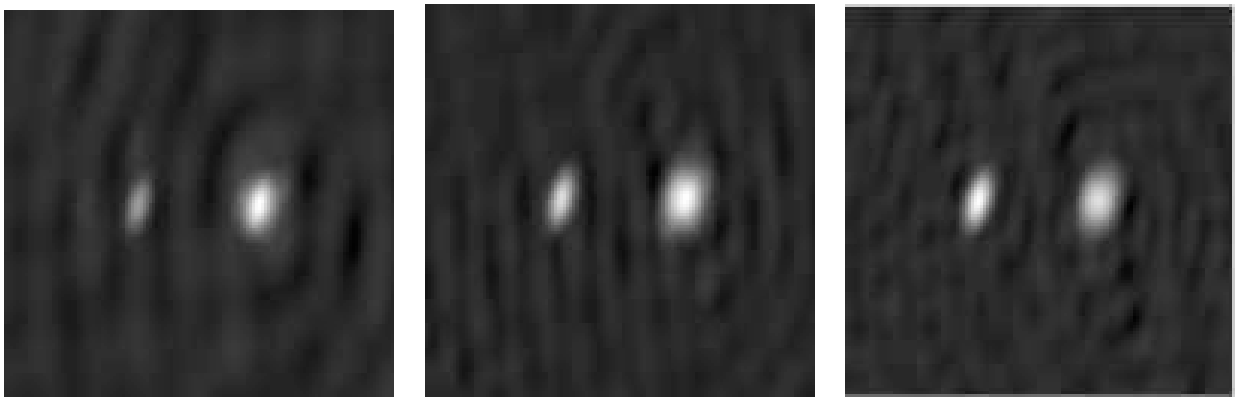

Figure 3. Three individual channel images from the red (left), middle, and blue (right) regions of the spectrometer ($\lambda\lambda = 800\text{nm} - 550\text{nm}$) based on the model shown in Fig. 2. These images are produced using the phase solution from the combined image in order to calibrate the (local) T_{eff} of each image pixel. The hot secondary (left component) can be seen to increase in brightness towards the blue.

6. CONVERGENCE AND PERFORMANCE

A critical issue is the behaviour of the algorithm under phase self-calibration. I have made the experience that with three baselines only (one closure phase), convergence is rather poor. Repeated deep CLEANing between self-calibration cycles helps convergence. However, this situation improves rapidly with more baselines. Fig. 4 shows that the original goal of producing superior images is met with simulated data.

7. APPLICATIONS

I have chosen to image the brightness variation of the surface of a rapidly rotating star, for which the parameterization of the flux as a function of wavelength based on blackbody emission is applicable, as in any other case

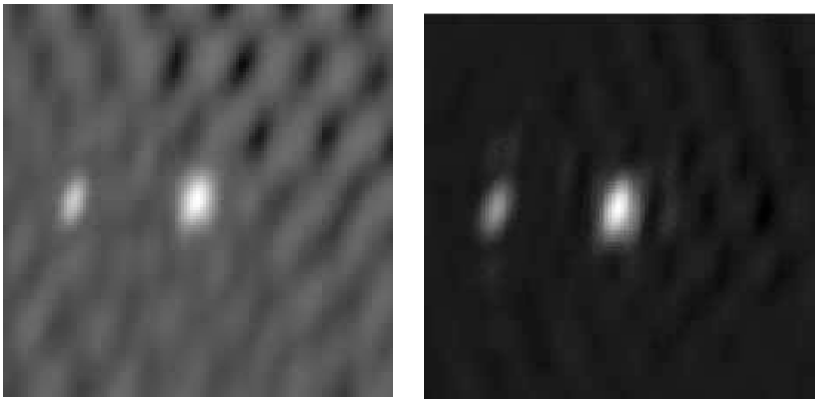

Figure 4. Comparison of a single channel image (left, higher background) and the combined (broadband) image of the binary.

involving optically thick emission, for example the thick dust structures (envelopes and accretion disks) around young stars.

For this simulation, I chose the NPOI array with the full 6-beam combiner for stations E7, W7, N7, AE, AW, and AN. It combines four different stations at a time in each of three spectrometers, covering the wavelength range from 850 nm to 550 nm (channel 1 to 16). The synthesized beam is about 1 mas in diameter.

The model used for Altair is the one from Peterson et al.[8] It produces a hot pole in the north-western quadrant of the stellar surface, and a gravity darkened equator. The stellar disk has a diameter of about 3 mas.

Due to the larger number of baselines, the algorithm converged through phase self-calibration much better than in the previous simulation. A small window was set around the stellar disk to prevent the subtraction of CLEAN components outside it. The results are shown in Fig. 5. What I call the combined CLEAN map is the result of the multi-channel CLEANing of the combined map. It provides a weight map for the summation of the blackbody spectra in order to derive flux maps for specific wavelengths ("image cube"). Due to hotter CLEAN components being much brighter than cool components, the combined CLEAN map shows a lower density ("intensity") where the hot pole of the rotating star is. In the image computed for the image cube from the combined and effective temperature maps shown in Fig. 5, the hot pole again corresponds to the brightest feature in the upper right quadrant of the stellar disk.

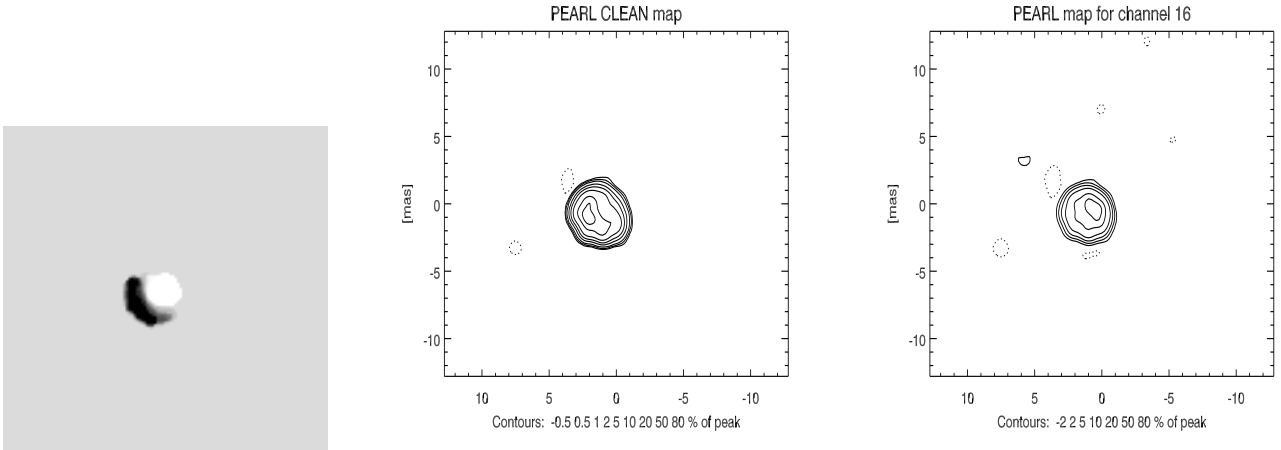

Figure 5. The derived effective temperature map (left), combined CLEAN map, and map of (the blue) channel 16 (right) for the rotating star simulation.

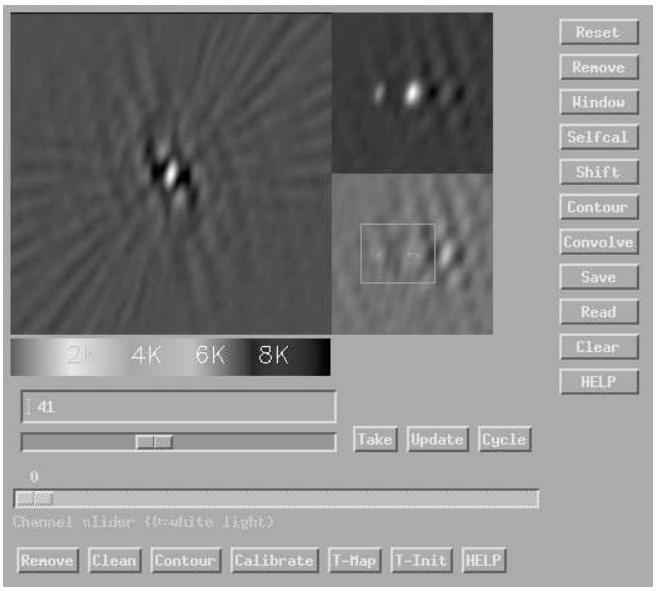

Figure 6. The layout of the main GUI of OYSTER/PEARL. The DM is displayed in the upper left, while the final map (CM + RM) and the CM are displayed in the right column. A slider (directly under the effective temperature color bar) is used to control the number of CLEAN iterations, while the slider below it is used to select the channel. A new phase self-calibration cycle is started when ever the Update or Cycle buttons are pressed, and the Calibrate button computes a new effective temperature map.

8. PUBLIC RELEASE

The code is available for download as part of the OYSTER data reduction package (*http://www.eso.org/∼chummel/oyster/oyster.html*). Figure 6 shows the main GUI.

REFERENCES

[1] Hummel, C. A., Benson, J. A., Hutter, D. J., Johnston, K. J., Mozurkewich, D., Armstrong, J. T., Hindsley, R. B., Gilbreath, G. C., Rickard, L. J., and White, N. M., "First Observations with a Co-phased Six-Station Optical Long-Baseline Array: Application to the Triple Star η Virginis," AJ **125**, 2630–2644 (May 2003).

[2] Armstrong, J. T., Mozurkewich, D., Rickard, L. J., Hutter, D. J., Benson, J. A., Bowers, P. F., Elias, II, N. M., Hummel, C. A., Johnston, K. J., Buscher, D. F., Clark, III, J. H., Ha, L., Ling, L., White, N. M., and Simon, R. S., "The Navy Prototype Optical Interferometer," ApJ **496**, 550–+ (Mar. 1998).

[3] Schmitt, H. R., Armstrong, J. T., Hindsley, R. B., and Pauls, T. A., "Understanding Cross Talk on the NPOI Multibeam Combiner," in [*The Power of Optical/IR Interferometry: Recent Scientific Results and 2nd Generation*], A. Richichi, F. Delplancke, F. Paresce, & A. Chelli, ed., 571–+ (2008).

[4] Le Bouquin, J., Lacour, S., Renard, S., Thiébaut, E., Merand, A., and Verhoelst, T., "Pre-maximum spectro-imaging of the Mira star T Leporis with AMBER/VLTI," A&A **496**, L1–L4 (Mar. 2009).

[5] Petrov, R. G., Malbet, F., Weigelt, G., and Antonelli, e. a., "AMBER, the near-infrared spectro-interferometric three-telescope VLTI instrument," A&A **464**, 1–12 (Mar. 2007).

[6] Haguenauer, P., Abuter, R., Alonso, J., and Argomedo, J. e. a., "The Very Large Telescope Interferometer: an update," in [*Society of Photo-Optical Instrumentation Engineers (SPIE) Conference Series*], *Presented at the Society of Photo-Optical Instrumentation Engineers (SPIE) Conference* **7013** (July 2008).

[7] Cornwell, T. J. and Wilkinson, P. N., "Selfcalibration," in [*Indirect Imaging. Measurement and Processing for Indirect Imaging*], J. A. Roberts, ed., 207–+ (1984).

[8] Peterson, D. M., Hummel, C. A., Pauls, T. A., Armstrong, J. T., Benson, J. A., Gilbreath, G. C., Hindsley, R. B., Hutter, D. J., Johnston, K. J., Mozurkewich, D., and Schmitt, H., "Resolving the Effects of Rotation in Altair with Long-Baseline Interferometry," ApJ **636**, 1087–1097 (Jan. 2006).